

**Appendices**

Appendices ..... 1

**Appendix A - Geophysical situation of the Noumea Lagoon ..... 2**

    Global geophysical context (from Ballu et al., 2019) ..... 2

5    Global and local hydrodynamic context ..... 3

    Sea level trends and vertical land movements in New Caledonia ..... 3

**Appendix B - Calibration of GEOCEAN-NC pressure gauges ..... 8**

**Appendix C - GNSS processing parameters ..... 10**

**Appendix D - Sea State Comparison between GNSS Buoy and 2019x pressure sensor ..... 11**

10    SWH from the GNSS buoy ..... 11

    SWH from the 2019x pressure sensors ..... 11

    SWH comparison ..... 11

    Tidal gradient between 2019x pressure gauge and buoy location ..... 14

**Appendix E – Along-track altimetric wet tropospheric corrections ..... 16**

15    **Appendix F - Validation of gradients from global geoid models in the lagoon ..... 19**

**Appendix G – Assessment of altimetry data quality in the lagoon ..... 21**

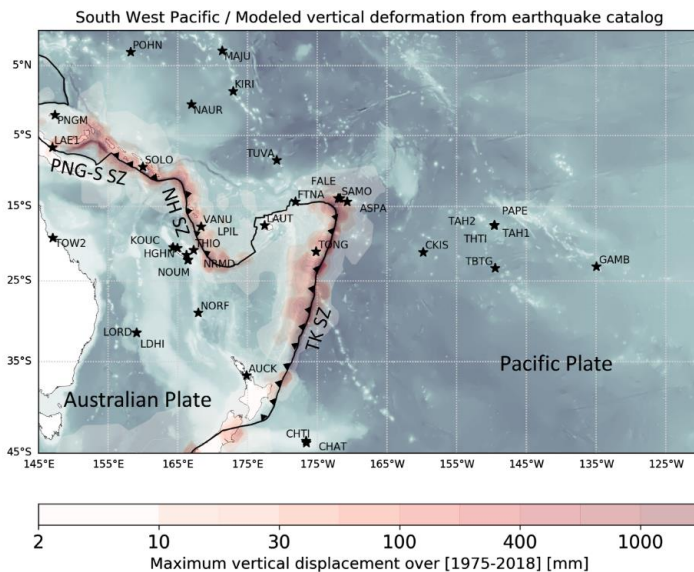
**References ..... 24**

## 20 Appendix A - Geophysical situation of the Noumea Lagoon

This appendix gives the geophysical context of our study based on the scientific literature.

### Global geophysical context (from Ballu et al., 2019)

Ballu et al. (2019) details the geophysical context of the South West Pacific zone (see Figure A1 for an overview). Focusing on our study area, the Noumea Lagoon is on an active tectonic zone on the Indo-Australian plate, that converge to the Pacific one at a mean rate of about 10 cm/y. There are two major subduction zones, and Noumea is near the New Hebrides and Papua-New Guinea—Salomon one, where the Australian plate is subducting. The contribution of non-tectonic processes to vertical displacement (i.e. subsidence of Pacific volcanoes and post-glacial isostatic adjustment) is estimated to be less than 1mm/y. It also appears that Noumea could be affected by earthquake, although neither strongly nor frequently.



30

35 **Figure A1.** Extracted from Ballu et al. (2019) – Stars represent stations with a long enough GPS record available (~7 yr). The background grey/blue shading highlights the bathymetric features in the oceanic domain, based on GEBCO 2014 (Weatherall et al., 2015) bathymetric data. The red shading indicates maximum absolute values of vertical displacement modelled using Okada (1985) dislocation model and the USGS earthquakes catalog for the period 1975–2018. The black line corresponds to the tectonic plate limit between the Australian Plate and the Pacific Plate, as proposed in the Morvel-25 plate boundary model (DeMets et al., 2010). The subduction zones are indicated by triangles on the over-riding plate, and labelled TK SZ, NH SZ and PNG-S SZ, respectively for the Tonga-Kermadec, New Hebrides and Papua-New Guinea—Salomon subduction zones.

### **Global and local hydrodynamic context**

40 There is a strong sea level regional variability in the western tropical Pacific area, mainly linked to the ENSO (El Niño-Southern Oscillation) with lower (resp. higher) sea level during El Niño (resp. La Nina) events, with differences in sea level around  $\pm 20\text{-}30$  cm (Becker et al., 2012). From the study of Garcin et al. (2016), it appears that periods that combine La Nina events and a negative Interdecadal Pacific Oscillation (IPO) lead to stronger trade winds and higher sea levels in the Lagoon. The climate component of sea level rise in Noumea is estimated to be around  $+0.5 \pm 0.5$  mm/y (Becker et al., 2012).

45

The lagoon surrounding New Caledonia is the world's largest lagoon, covering about 20,000 km<sup>2</sup>. A barrier reef separates the lagoon from the Pacific Ocean, at a distance from the coast ranging from 5 km in its northern part to 40 km in its southern part. Deep passes intersect the coral reef and let the ocean flow in and out. During low tides, the crest of the reef can emerge.

50 The southern part of the lagoon, near Noumea city has an average depth of 15-20 m. Its dynamics is dominated by semi-diurnal tides, with a tidal range varying from about 1.4 m at spring tides to 0.6 m at neap tides (Douillet, 1998). Part of the offshore oceanic signal enters the lagoon through deep passes, but it is then strongly attenuated inside the Lagoon by wave breaking and friction on the reef flat (Bonneton et al., 2007).

55 To a first approximation, the sea state in the lagoon is mainly dominated by the wind sea (Jouan et al., 2009). Aucan et al. (2017b) identify three types of waves in the lagoon: (1) low-frequency swell waves (8-25 s) generated offshore (SSW) and then impacting the barrier reef, (2) high-frequency waves (3-8 s), generated inside the lagoon by the prevailing trade winds (SE), and (3) infragravity waves (20-500 s) that can be similarly energetic on the islet reef flat. The wave impact on the islands depend on their location and distance to the coral reef and the main passes, and is modulated by tidal level and the surrounding reef plate (Aucan et al., 2017b; Garcin et al., 2016).

60

Finally, it is possible that wave breaking on the barrier reef could induce a localized elevation of the water body behind the reef (i.e. setup), which would be evacuated through the passes and would not necessarily reach the coast and thus the tide gauge. This phenomenon was observed during the passage of tropical cyclone COOK in 2017 (Jullien et al., 2020). However, in previous publication based on in-situ data in the lagoon (Aucan et al., 2017b), no significant setup was observed (Aucan pers. communication).

65

### **Sea level trends and vertical land movements in New Caledonia**

In New-Caledonia, the sea level evolution is still an issue as altimetry, tide gauge and land-based GNSS station do not provide consistent information (Aucan et al., 2017a, Martínez-Asensio et al., 2019 and tables A1 and A2 for an overview of the values).

70 Over the altimetry period (1993-2013), Aucan et al. (2017a) find a sea level trend difference between tide gauge and altimetry

of  $+1.4 \pm 0.7$  mm/y. Ideally, these residuals movements could be explained by Vertical Land Movements (VLM). However, nor VLM estimated by GIA models (i.e.  $\sim -0.1$  to  $-0.3$  mm/y in the area from the ICE6G-VM5a model - Peltier et al., 2015), nor VLM estimation from permanent GNSS stations (Table A2), could explain the uplift inferred by altimetry minus tide gauge measurements.

75

Several hypotheses could be considered to explain this:

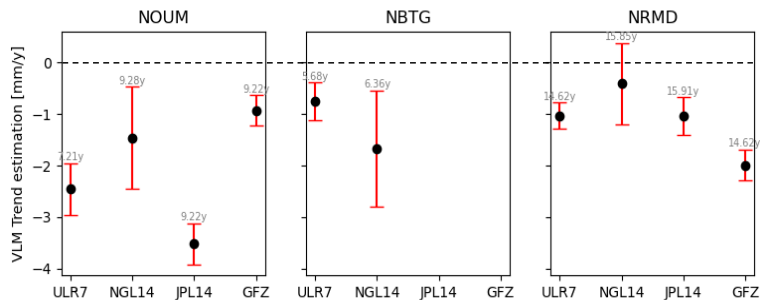
80

1. A water level elevation between the altimeter sampling point and the tide gauge position (i.e. setup), which does not appear to be significant in the lagoon (see previous section for more details).
2. Mis-modeled discontinuities in the GNSS time series can result in an incorrect estimate of VLM. In their comparative study of different GNSS solutions, Ballu et al. (2019) find that the estimation of VLM trend for the NRMD station is very sensitive to the integration (or not) of a discontinuity during a material change in the middle of the time series. The methodology used to compute the trend and the period considered also impact the final result (see Table A2 and figure A2 for the different estimates of VLM at GNSS stations, and Figure A3 for time series comparison at NOUM station).

85

3. We can also consider the processing of altimetry data. For now, the data used in the tide gauge comparison are derived from gridded products integrating standard corrections that may not be appropriate for coastal locations. Aucan et al. (2017) altimeter point selected for comparison is located 95 km from the tide gauge. When considering the variability of sea level trends seen by altimetry in this area (Figure A4), one wonders if the selection of a point so far from the tide gauge is appropriate.

90



95 **Figure A2.** VLM trend estimation at three GNSS station in Noumea from 4 different solutions : SONEL-ULR7 solution from Gravelle et al. (2022) / NGL - NGL14 solution from Blewitt et al. (2016) / JPL - JPL14 solution from Heflin et al. (2020) / GFZ – GT3 solution from Männel et al. (2022). The red bar represents the uncertainty associated with each estimate, and the number shows the length of the observation years used to estimate the trend.

**Table A1.** Tide gauges Relative Sea Level trends estimates in New Caledonia from different studies

Relative Sea Level	TG	Station name	Period	Trend [mm/y]	Source
		Noumea	1957-2015	$0.8 \pm 0.4$	Aucan et al., 2017a
	1993-2015	$2.2 \pm 1.6$			
RESL <sup>1</sup> - GNSS	TG	Noumea A	1967-2015	$0.9 \pm 0.4$	Martínez-Asensio et al., 2019
			1993-2015	$2.4 \pm 1.0$	
		Ouinne	1981-2015	$1.7 \pm 0.3$	
		Lifou	2011-2015	$-5.0 \pm 9.7$	
		Noumea	1967-2003	$2.6 \pm 0.6$	Becker et al., 2012

100

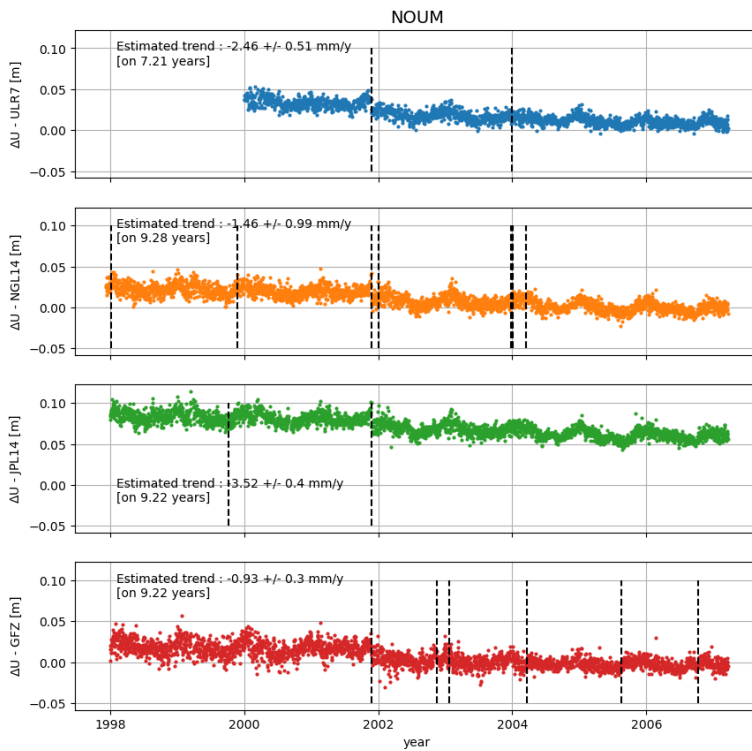
**Table A2.** Vertical Land Movements trends estimates in New Caledonia from different studies.

Vertical Land Movements	GNSS	Station name	Period	Trend [mm/y]	Source	
		NOUM			1997-2007	$-1.4 \pm 0.3$
			-	$-2.1 \pm 0.2$	Becker et al., 2012	
			-	$-1.3 \pm 0.7$	Ballu et al., 2019	
			2000-2007	$-2.5 \pm 0.5$	SONEL – ULR7 <sup>2</sup>	
			1998-2007	$-1.5 \pm 1.0$	NGL - NGL14 <sup>2</sup>	
			1998-2007	$-3.5 \pm 0.4$	JPL - JPL14 <sup>2</sup>	
			1998-2007	$-0.9 \pm 0.3$	GFZ – GT3 <sup>2</sup>	
			1998-2007	$-1.5 \pm 1.0$	Hammond et al., 2021	
NRMD				-	$-1.3 \pm 0.6$	Ballu et al., 2019
				2006-2020	$-1.0 \pm 0.3$	SONEL – ULR7 <sup>2</sup>
				2006-2021	$-0.4 \pm 0.8$	NGL - NGL14 <sup>2</sup>
				2006-2021	$-1.0 \pm 0.4$	JPL - JPL14 <sup>2</sup>
				2006-2020	$-2.0 \pm 0.3$	GFZ – GT3 <sup>2</sup>
NBTG				2006-2023	$-0.5 \pm 0.6$	Hammond et al., 2021
			2015-2020	$-0.7 \pm 0.4$	SONEL – ULR7 <sup>2</sup>	
			2015-2021	$-1.7 \pm 1.1$	NGL - NGL14 <sup>2</sup>	
YATE			2015-2022	$-1.7 \pm 1.2$	Hammond et al., 2021	
			2008-2016	$1.7 \pm 1.7$	Martínez-Asensio et al., 2019	
LPIL			1996-2016	$-0.2 \pm 0.4$		
			-	$-0.7 \pm 0.7$	Ballu et al., 2019	
THIO			-	$-2.0 \pm 0.7$	Hammond et al., 2021	
			2008-2023	$-1.8 \pm 1.2$		
KOUC			-	$-0.9 \pm 0.6$	Ballu et al., 2019	

<sup>1</sup> RESL = Reconstructed Sea Level (see Becker et al., 2012 for more details)

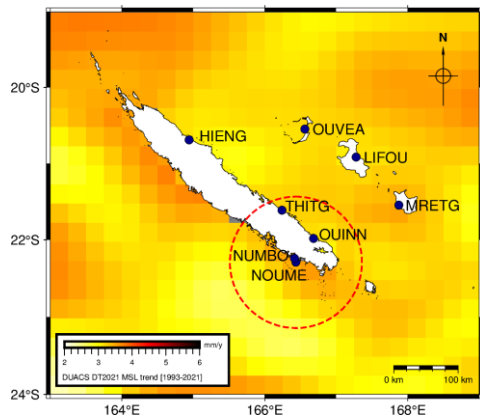
<sup>2</sup> GNSS VLM sources : SONEL-ULR7 solution from Gravelle et al. (2022) / NGL - NGL14 solution from Blewitt et al. (2016) / JPL - JPL14 solution from Hefflin et al. (2020) / GFZ – GT3 solution from Männel et al. (2022)

	Altimetry-TG	HGHN	-	$-1.3 \pm 0.6$	Hammond et al., 2021	
			2010-2023	$-1.7 \pm 1.2$		
		Noumea	1993-2013	$1.4 \pm 0.7$	Aucan et al., 2017a	
			1957-2010	$1.4 \pm 0.4$		
			1993-2001	$2.5 \pm 1.5$	Nerem and Mitchum, 2002	
	VLM@TG (from GNSS station interpolation)	Chaleix	1967-2015	$1.7 \pm 0.2$	Martínez-Asensio et al., 2019	
			-	$-1.7 \pm 0.3$	Hammond et al., 2021	
			Numbo	-		$-1.7 \pm 0.4$
			Ouinne	-		$-1.8 \pm 0.4$
		Lifou	-	$-3.1 \pm 1.1$		



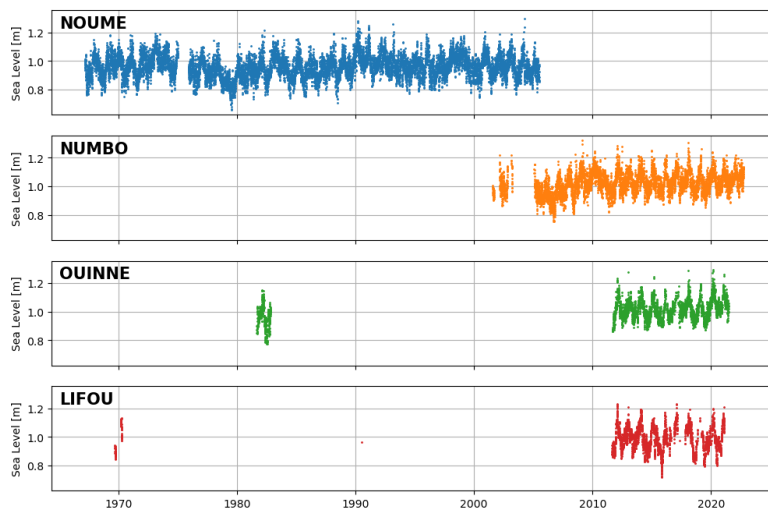
105

**Figure A3.** Time series used to estimate VLM trend at the NOUM station for the 4 solutions presented in Figure G2. The dashed vertical bar indicates the discontinuity considered by each solution to compute the final trend.



110

**Figure A4.** Location of the main TG sites in New-Caledonia. The background shows the merged gridded regional mean sea level trends from DUACS DT2021 over [1993-2021] (CLS/CMEMS). The red dotted circle with 95km radius represent the distance between Noumea tide gauge and altimetry grid node used in Aucan et al., 2017a study for comparison.



115

**Figure A5.** Overview NOUME/NUMBO/QUINNE/LIFOU tide gauges daily sea level means from SONEL portal.

## Appendix B - Calibration of GEOCEAN-NC pressure gauges

Pressure sensors are known to drift over time. This drift is generally considered to be linear and variable from instrument to instrument, depending on the age and past history of the sensor. In our case, a calibration session in hyperbaric chamber before and after their deployment do not show a clear instrumental drift of the different sensors (Figure B1c).

To verify the stability of the measurements during the 13 months of immersion, we compute relative differences with the 2019o sensor (Figure B1d). This sensor was chosen as a reference because of its installation on a stable support (coral reef), and we consider its instrumental drift negligible regarding the previous calibration session. Results show that, for sensors 2019i and 2019j (Figure B1d, in green and yellow), differences do not show a significant trend: therefore, it is assumed that these two sensors remained stationary.

On the contrary, the 2019o/2019r difference (Figure B1d, in red) shows a negative trend for the first 7 months, before stabilizing in May 2020. This suggests a sinking of the sensor into the sand, which was confirmed by the divers during the gauge's recovery. The nature of the bottom is therefore a parameter to consider when deploying the sensors. If the experimental conditions impose an installation on very soft grounds, other types of support can also be considered (suction anchors, etc.).

Finally, the 2019o/2019x difference (Figure B1d, blue) shows a linear trend of about  $-70$  mm/yr, which is not visible on the other sensors nor conceivable from the pre- and post-deployment drift checks. This could indicate continued sensor sinking, and in the absence of further information, we chose to correct for this trend in the following study.

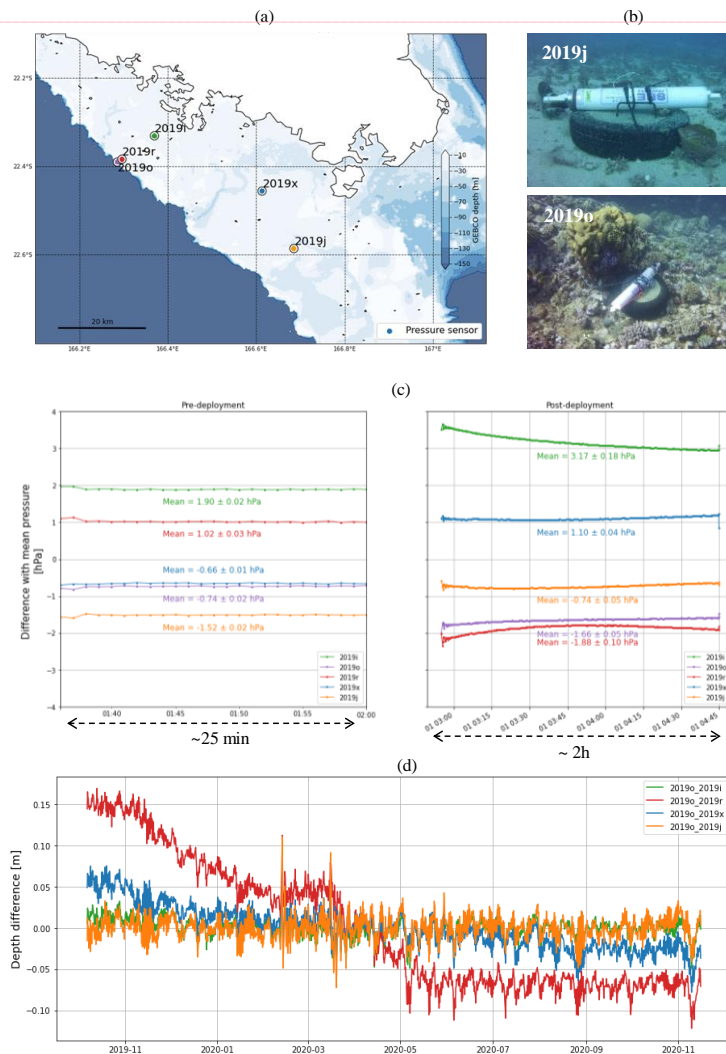


**Figure B1.** Installation and calibration phase of the pressure gauges / (a) – (b) Location and mooring of the 5 pressure gauges deployed during GEOCEAN-NC campaign. / (c) Hyperbaric chamber calibration results: difference between SBE observations and mean pressure at 10m before (left) and after (right) deployment. For conversion, 1 hPa ~ 1 cm of water. / (d) Difference between the 2019o sensor time series and the other 4 pressure sensors. The pressure time series were transformed into equivalent water depths and then corrected for tide using harmonic analysis. The final differences were filtered with a sliding average (6 h windows, 6 h steps).

**Commenté [CC1]:** figure c – post-deployment : green and red still appear quite variable in time? is this expected over two hours?

figure d - comment on the nonlinear red curve in the paper?

**Commenté [CC2R1]:** The red curve is related to the 2019r sensor, which is not used in our analyse, so we don't describe this curve in the main paper. However, we describe this phenomena on the upper paragraph for readers interesting in this results :

See : "On the contrary, the 2019o/2019r difference (Figure B1d, in red) shows a negative trend for the first 7 months, before stabilizing in May 2020. This suggests a sinking of the sensor into the sand, which was confirmed by the divers during the gauge's recovery."

## Appendix C - GNSS processing parameters

140 Table C1. GINS parameters for GNSS computation<sup>3</sup>

	GNSS Buoy	CalNaGeo GNSS carpet
Antenna model	TRM115000.10 NONE	TRM125000.30 NONE
Receiver model	SEPT POLARX5	SEPT POLARX5
Constellation(s) used	GPS / GLONASS / GALILEO	GPS / GLONASS / GALILEO
Resolution mode	IPPP / PPP / IPPP	PPP
Observation sampling	10s (i.e. 1 obs./10s)	10s (i.e. 1 obs./10s)
Orbit/Clock products	MG3 <i>(30s products, linearly interpolated for higher frequencies data)</i>	MG3 <i>(30s products, linearly interpolated for higher frequencies data)</i>
Macromodel	Nominal MG3	Nominal MG3
ANTEX	igsR3_2077.atx	igsR3_2077.atx
Earth parameters	Nominal NRO	Nominal NRO
Ocean tide loading	FES2014	FES2014
Solid earth tide	IERS 2010 convention <i>(cyclic and permanent component)</i>	IERS 2010 convention <i>(cyclic and permanent component)</i>
Atmosphere loading	Uncorrected	Uncorrected
Ocean tide	Uncorrected	Uncorrected
Mean sea surface	Uncorrected	Uncorrected
Center of mass correction	Uncorrected	Uncorrected
Tropospheric correction	IERS 2010 convention <i>(wet, wmf1, gpt2)</i>	IERS 2010 convention <i>(wet, wmf1, gpt2)</i>
Ionospheric correction	Second order ionospheric correction (Hernández-Pajares et al., 2007)	Second order ionospheric correction (Hernández-Pajares et al., 2007)
Elevation mask	15	15
Minimum visible satellite	4	4
Minimum satellite pass duration	300 s	350 s
Epochs deleted at each pass start	2 (20 sec)	2 (20 sec)
Minimum pass length for integer ambiguity computation	600 s	-
Kalman filter	Yes (more details about the algorithm in Barbu et al., 2018)	Yes (more details about the algorithm in Barbu et al., 2018)

Commenté [CC3]: again, 10 Hz or 1 per 10 seconds?

Commenté [CC4]: What is the default model used ?

Commenté [CC5]: more info required here - process noise? how is trop dealt with?

Commenté [CC6R5]: We have updated the table with the elements in our possession, in particular on the methods used for the ionospheric and tropospheric corrections. However, we do not have enough understanding of the whole processing to be able to detail the process noise.

<sup>3</sup> For more details about the GINS software, see GRGS, 2018; Marty et al., 2011. The reader may also refer to the paper of Kouba, 2015 for a description of the different parameters and models that can be used in the GNSS computation process.

## 145 **Appendix D - Sea State Comparison between GNSS Buoy and 2019x pressure sensor**

To be sure that the GNSS buoy and the 2019x pressure sensor monitor the same sea, we compare the Significant Wave Heights (SWH) from both instruments. As they are located 4km apart, we also used tide model predictions at both locations to compute a tidal gradient between both sensors.

### **SWH from the GNSS buoy**

150 Located at the water surface, the GNSS buoy observations are directly impacted by the sea state, but also by longer variations such as tide or the geoid. To process these data, we used the method describe in Bonnefond et al. (2003). To focus on the short variations, we differentiate between the filtered and the raw buoy data (RTKLib 1Hz differential solution). For that, GNSS heights are filtered using the Vondrak filter (Vondrak, 1977) with a cut-off period of 120s to remove short-wavelength oscillations (Figure D1a). Standard deviation of the residuals' heights ( $\sigma_{shr}$ ) is compute using a 120s period's running average  
155 (Figure D1b). The standard deviation of the buoy due to waves ( $\sigma_{wave}$ ) is then equal to:  $\sigma_{wave} = \sqrt{\sigma_{shr}^2 - \sigma_{gps}^2}$  with  $\sigma_{gps}$  an estimation of the GNSS buoy processing errors (here estimate to be 2.5cm). The final Significant Wave Height (SWH) at the buoy is then derived from:  $SWH = 4 \times \sigma_{wave}$  (Figure D1c).

### **SWH from the 2019x pressure sensors**

The SBE26plus sensors have been set up to measure wave bursts during 10 minutes every hour (with 1 second wave sample  
160 duration). To compute the resulting SWH from these wave bursts at 2019x, we first transform pressure records to equivalent hydrostatic depths atmospheric pressure time series from ERA5 (Hersbach et al., 2018) at the pressure gauge location, temperature from pressure recorder and a mean salinity of 35.5 psu. Then, we remove a linear trend for each burst of 512 values and reconstruct waves elevation. The Power Spectrum Density (PSD) is then estimated and the final waves parameters are extracted. After several tests, we choose a cut-off frequency of  $F_c=0.25$  Hz. In order to easily compare with GNSS buoy  
165 SWH, this method is applied to the buoy observations, after selecting the same observation windows as from the pressure sensor's wave bursts.

### **SWH comparison**

The results of the GNSS Buoy and 2019x pressure sensor SWH computation are showed in Figure D3a. We can see that the GNSS buoy, measuring at the direct water surface, is very sensitive to waves, down to frequency bands of 0.5Hz. If we apply  
170 the same cut-off frequency as the bottom pressure sensor ( $F_c=0.25$ ) to the buoy data, we obtain a high correlation between the two series ( $c=0.914$ , Figure D3b). Thus, at a depth of around 20 m, the pressure sensor is limited to a narrower frequency band than the buoy. But if we limit the comparison at the frequency band common to both systems, they roughly see the same sea.

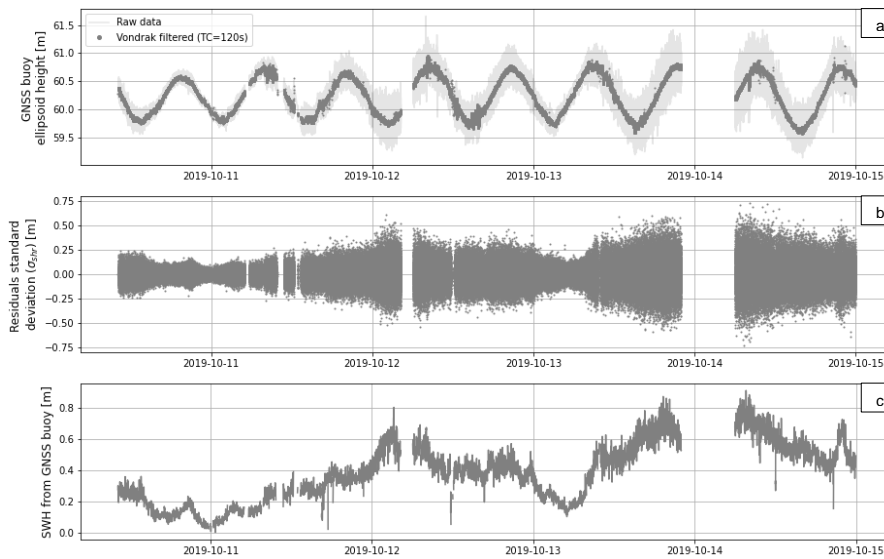


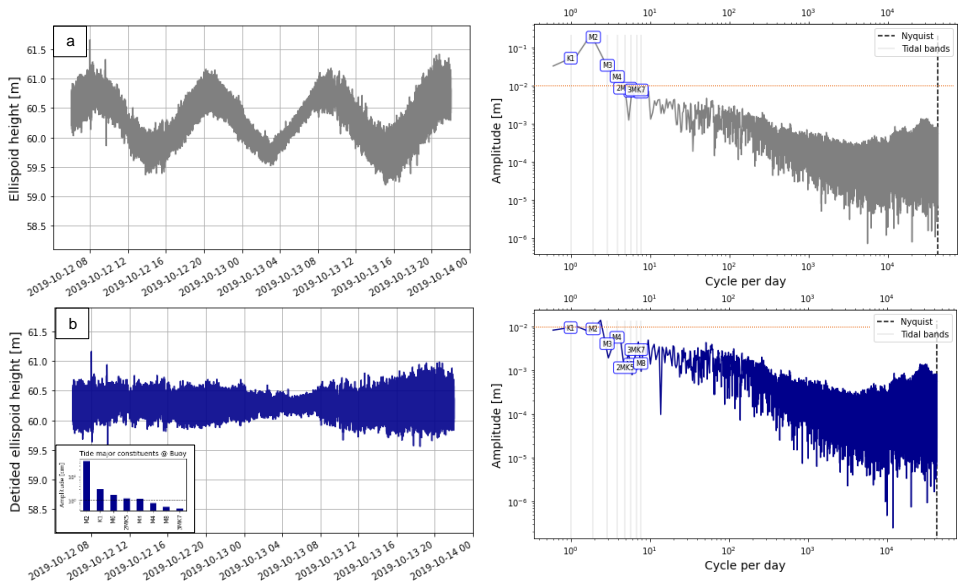
**Figure D1.** Computation step of the GNSS Buoy SWH / (a) Raw and Vondrak filtered GNSS buoy ellipsoid heights / (b) Standard deviation of the residuals' heights computed on 120s window ( $\sigma_{str}$ ) / (c) Significant Wave Height (SWH) at the buoy position.

**Commenté [CC7]:** a - I'm not convinced about the quality of the GNSS solution - what are these oscillations? (upper panel 2019-10-11 ~9h)

c - the scale here doesn't look right. The residuals are typically 0.5 m, 4 x std of those is wave more than 0.2 ??

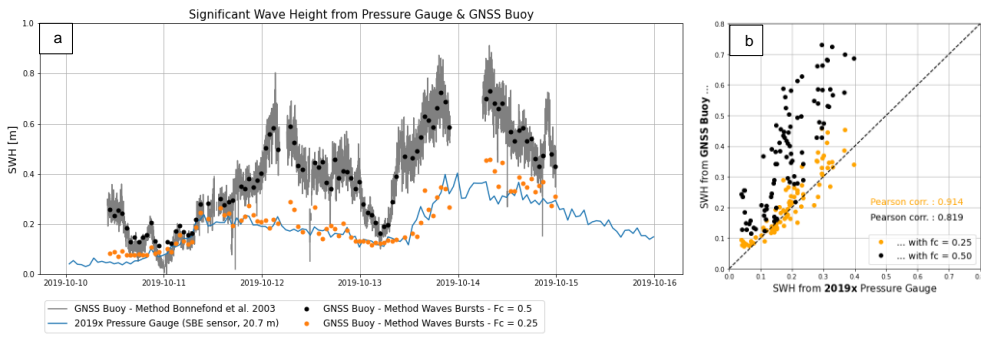
**Commenté [CC8R7]:** Indeed, in the solution presented previously, we had not filtered the positions that were not fixed. We have updated the curves considering this parameter. We are also aware that this solution is the result of a differential computation with a base station located several tens of km away, which limits the quality of our positioning.

Concerning panel c, the multiplication by 4 was indeed missing, which changed the scale. Thank you for noticing it!



180 **Figure D2.** FFT computation for GNSS buoy observations of the 12<sup>th</sup> - 13<sup>th</sup> October 2019 / (a) GNSS buoy ellipsoid heights over the period (left panel) and its corresponding FFT (right panel) / (b) GNSS buoy detided ellipsoid height (left panel) with the amplitude of the major tide constituents at the buoy location and its corresponding FFT (right panel). Note that for the two FFT plot, the red dotted line highlights the 10 cm amplitude.

Commenté [CC9]: more detail needed for this plot - de tide first so you can see residual power bands.  
 Commenté [CC10R9]: We complete the figure with the detided time series and its FFT.



185 **Figure D3.** (a) Significant Wave Height from GNSS Buoy (grey line) and 2019x pressure gauge (blue line). To allow direct comparison, the GNSS Buoy SWH is also compute with the wave burst method, using different cut-off frequencies (black and orange points). / (b) Correlation between 2019x Pressure Gauge and GNSS Buoy SWH.

### Tidal gradient between 2019x pressure gauge and buoy location

Although only 4km apart, the GNSS buoy and the pressure sensor may be subject to slightly different tidal regimes. We therefore used the output of the SCHISM hydrodynamic model, provided by Jérôme Lefevre from IRD in Noumea, to compute the tidal gradient between the two positions.

190

Figure D4 represents these results: the bar plots on the left panel shows the model extraction of amplitude and phase of the main tidal constituents at the buoy (blue) and pressure sensor location (orange). Differentiating the tide constituents [PG - Buoy], we obtain the amplitude and phase of the tidal gradient (red). The tide reconstruction due to this tidal gradient is showed in Figure D4c. We can see that over the 3 days of the GNSS buoy deployment, we could have height differences up to  $\pm 1$  cm

195

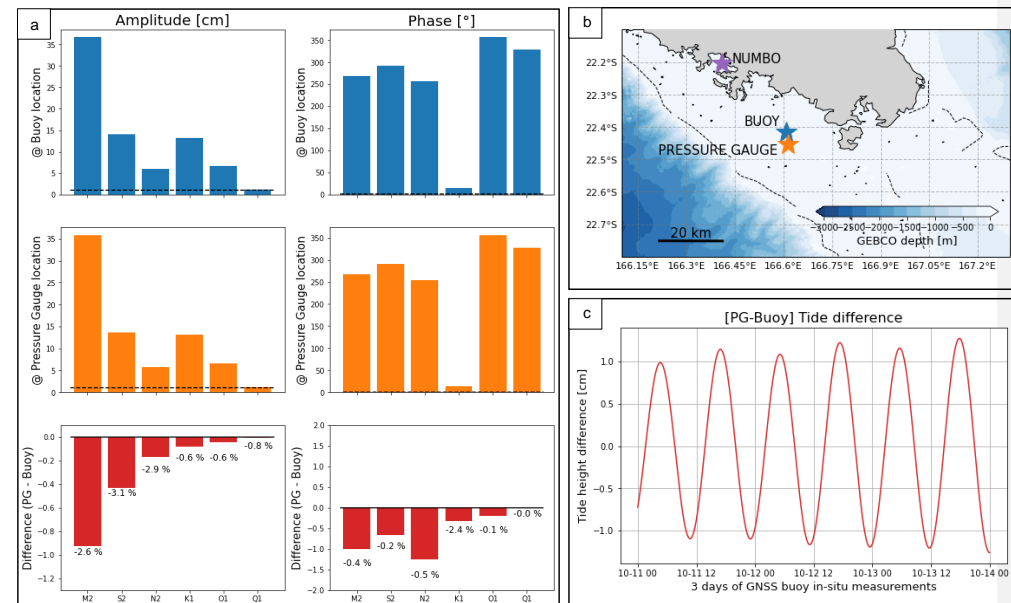
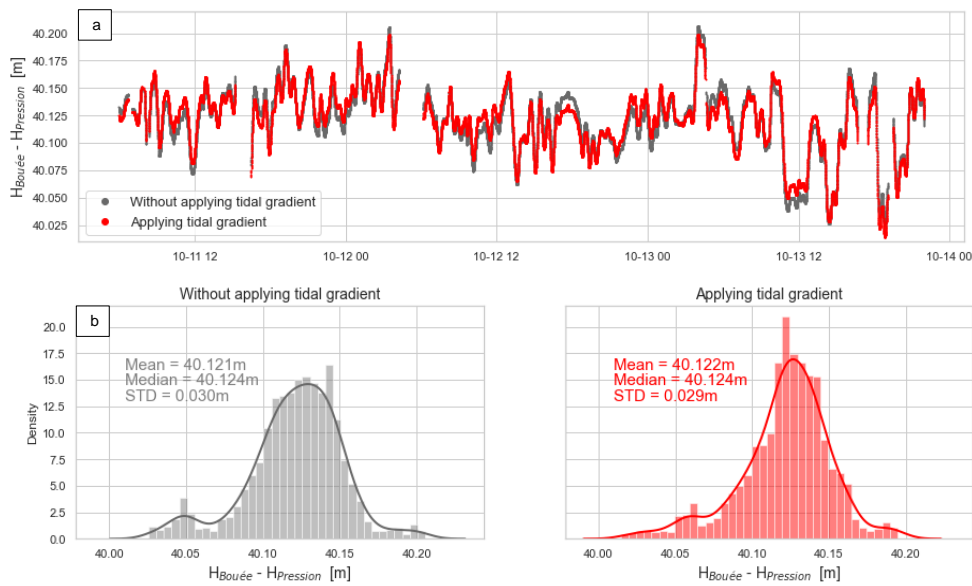


**Figure D4.** (a) Amplitude and phase of the six main tide constituents extracted from SCHISM hydrodynamic model at the buoy (blue) and pressure gauge location (orange). The red bar plot show amplitude and phase of the tide gradient between these two points. / (b) Location of the sensors. Note stars colours correspond to bar plot colours. / (c) Tide reconstruction over the 3 days of the GNSS buoy measurements using amplitude and phase of the tide gradient.

200

205 These values are not negligible in our case, where we aim to get closer to the cm-level. Figure D5 represents the water heights difference observed by the GNSS buoy and the pressure sensor (see Section 3.3 for more details), considering or not this tidal gradient. When comparing histograms of the residuals (Figure D5b), we can see that adding the gradient improves the distribution of the residuals, without impacting the mean bias. We have subsequently considered this tidal gradient to correct the observations of our pressure sensor.



210 **Figure D5.** (a) Height difference over the 3 days of common observation period between the GNSS buoy and the pressure gauge (see Section 3.3 for more details) considering (in red) or not (in grey) the tide gradient between the two locations. / (b) Histograms of the GNSS buoy and pressure gauge differences without (left panel – grey) or with (right panel – red) tide gradients.

## Appendix E – Along-track altimetric wet tropospheric corrections

215 In the lagoon, the effect of coastal contamination on the radiometer data is visible when approaching the main island (Figure E1, grey area). However, the wet tropospheric correction seems to be exploitable at our comparison point for all missions (Figure E1, red area).

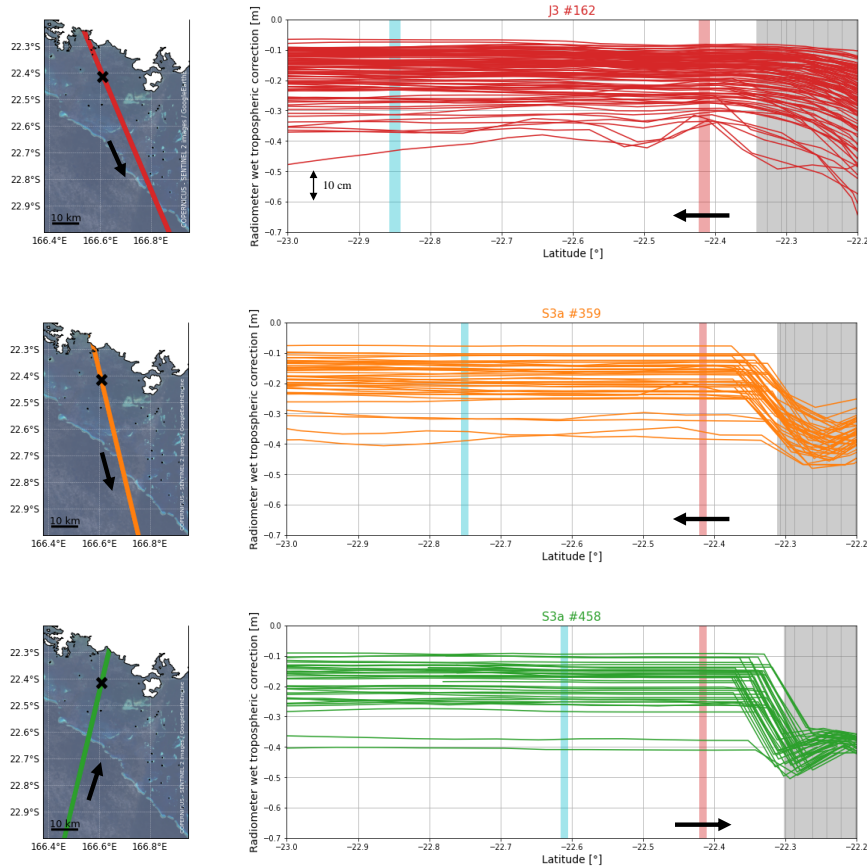


**Figure E1.** Evolution of the radiometer correction along the altimetric tracks used in our study (red for Jason 3 #162, orange for Sentinel-3a #359 and green for Sentinel-3a #458). The grey vertical bar represents the main island overfly, the red vertical bar represents the comparison point location and the blue vertical bar corresponds to the reef barrier overfly. Arrows symbolize the satellite direction of flight.

Commenté [CC11]: show the CP as a dot on the map.

the same plot but showing ECMWF-radiometer would be interesting to show

Commenté [CC12R11]: We complete the figures to show the crossover on the map and also add Figure E1 showing ECMWF-radiometer evolution along track.

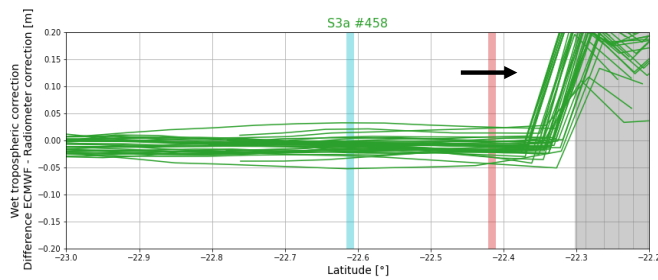
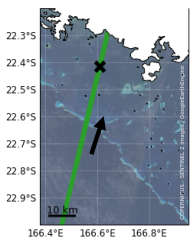
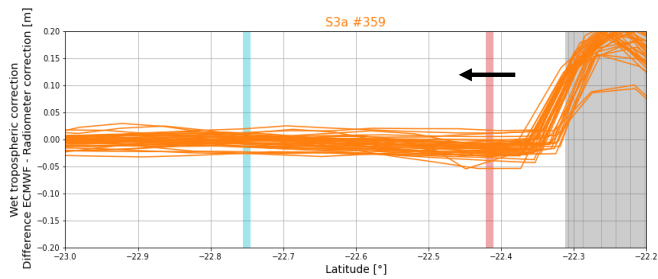
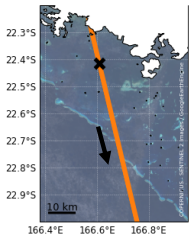
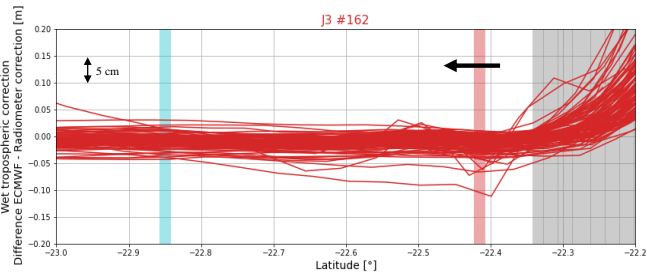
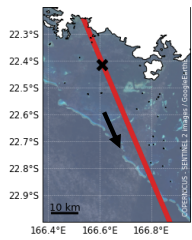


**Figure E2.** Evolution of the difference between ECMWF and the radiometer correction along the altimetric tracks used in our study (red for Jason 3 #162, orange for Sentinel-3a #359 and green for Sentinel-3a #458). The grey vertical bar represents the main island overfly, the red vertical bar represents the comparison point location and the blue vertical bar corresponds to the reef barrier overfly. Arrows symbolize the satellite direction of flight.

To test this hypothesis, we compared the correction provided by the radiometer with two data sets: (1) the wet tropospheric correction from the ECMWF model and (2) the wet tropospheric correction computed from permanent GNSS stations in Noumea. For the latter, we used the total tropospheric delay extracted from GINS PPP computations, performed by the CNES teams in Toulouse, for the NRMD and NOUM stations. The tropospheric corrections, estimated every 2 hours, are interpolated at the satellite pass times. The dry tropospheric component from GDR files is then subtracted to finally obtain the wet component of the tropospheric correction. Since the GNSS stations are not at sea level elevation, an additional correction is applied to account for the pressure difference with the comparison point (which is at sea level elevation). For this, we used the Saastamoinen equations (Saastamoinen, 1972) according to the method described by Kouba (2008).

To illustrate the objective of our comparison, we represent the wet tropospheric delay from radiometer, ECMWF model and GNSS data along the Jason 3 track #162 for 3 random cycles (Figure E3). If we focus on our study area (the grey area on Figure E3), we can see that the three solutions can be very variable according to the cycles and can affect the estimate of the altimetric SSH at the centimetric level.

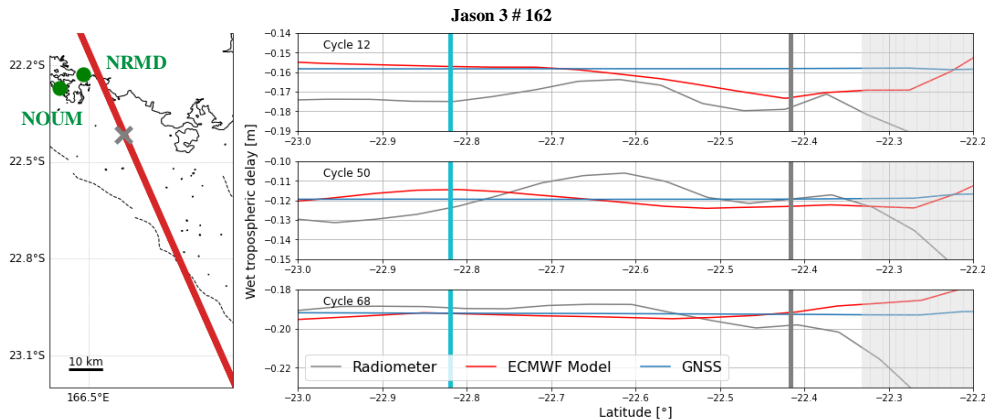


**Figure E3.** Wet tropospheric correction from radiometer (grey), ECMWF model (red) and GNSS stations (blue) for three random cycles of the Jason 3 #162. On the right panel, the light grey area represents the main island overfly, the dark grey area represents the comparison point overfly and the blue area corresponds to the reef barrier overfly.

## Appendix F - Validation of gradients from global geoid models in the lagoon

Another objective of the cruise was to improve sea level kinematic mapping methodology in coastal areas through the deployment and comparison of multiple sensors, as described in Chupin et al. 2020. For that purpose, the coastal version of the CalNaGeo GNSS carpet was towed by R/V ALIS along and across altimetry tracks, and inside and outside the lagoon (Figure 1b, blue lines). The 10s observations of CalNaGeo were processed with GINS in PPP mode (Marty et al., 2011) (processing details in Appendix C), and filtered using the Vondrak filter with a cutoff period of 30 min (~ 5.4 km at 6 knots). The 2019x pressure sensor is then used to remove the time-varying component of CalNaGeo measurements (especially the oceanic tide), assuming that it does not vary spatially over our area). Thanks to these data, we then analyse the performance of different models to estimate geoid gradients.

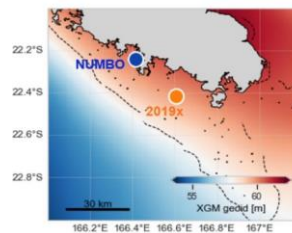
Three datasets were selected to conduct our comparison:

- The XGM2019e global gravity field model (Zingerle et al., 2020), represented by spherical harmonics corresponding to a spatial resolution of 2' (~4 km). This model is based on GOCO06s satellite data combined with terrestrial measurements for shorter wavelengths. Gravity anomalies derived from satellite altimetry are used over oceans (DTU13).
- The global Earth gravity potential model EGM2008 (Pavlis et al., 2012) defined on a 5' arc (~10 km) equiangular grid. This model is based on terrestrial, altimetric and airborne gravity data.
- An average model of the Earth's gravity field, the EIGEN-GRGS.RL04.MEAN-FIELD (Lemoine et al., 2019), hereafter referred as EIGEN, computed from the RL04 GRACE+SLR monthly time series and GOCE data.

Along CalNaGeo track, the comparison with XGM2019e and EGM08 gradients shows no significant differences (resp. Fig. F1b and F1c). On the contrary, the comparison with the EIGEN model shows a residual southeast/northwest gradient of about 1.8 cm/km (Figure F1d). In our process, we thus select the XGM2019e model to account for geoid gradients. This first study allowed us to select the most relevant model for our area, but further analysis is still required to refine the CalNaGeo GNSS solution and to map the mean sea surface over the whole lagoon.

**Table F1. Geoid height difference between 2019x pressure gauge (4 km south of the crossover) and Noumea tide-gauge site**

	Geoid height difference
<b>XGM 2019e</b> (Zingerle et al., 2020)	-52.4 cm
<b>EGM 2008</b> (Pavlis et al., 2012)	- 54.9 cm
<b>EIGEN</b> (Lemoine et al., 2019)	- 27.0 cm
<b>Our study</b> ( $\Delta datum_{TG \rightarrow PG}$ )	- 57.1 cm

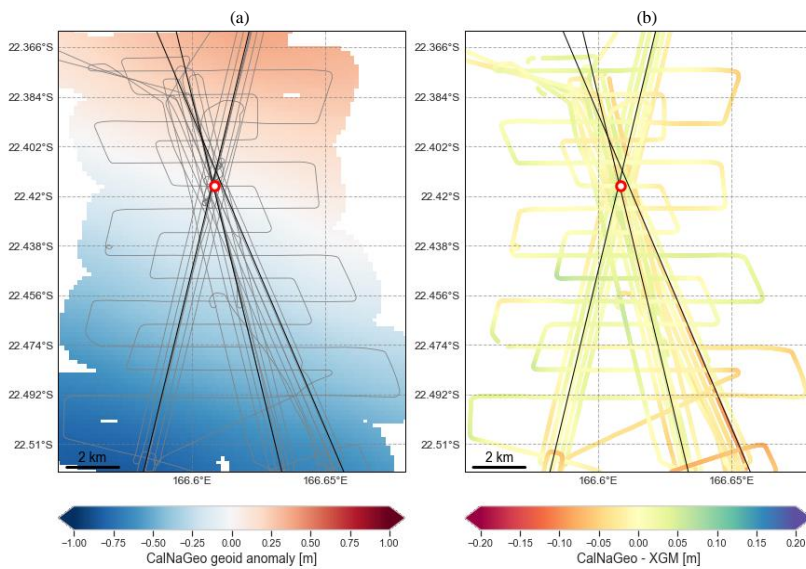


Commenté [CC13]: doesn't this assume the tide does not vary spatially...

Commenté [CC14]: s4 km south of 2019x

260

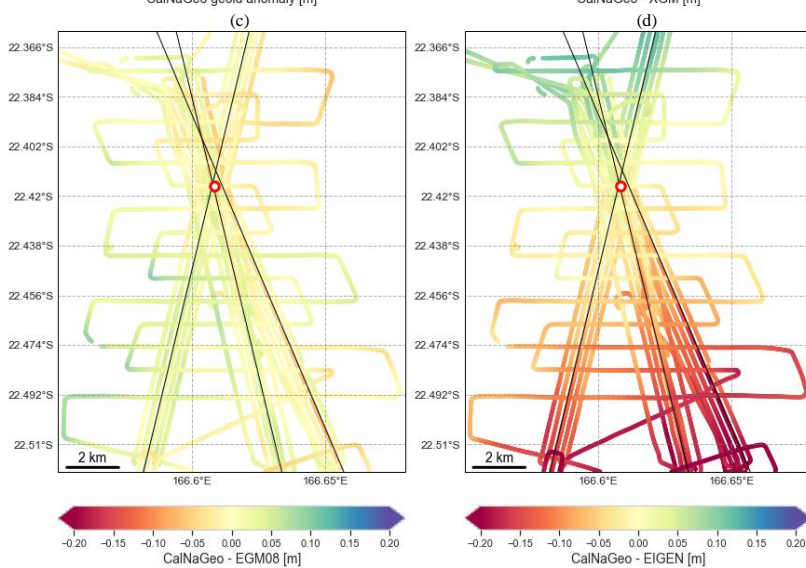
265



270

275

280



70

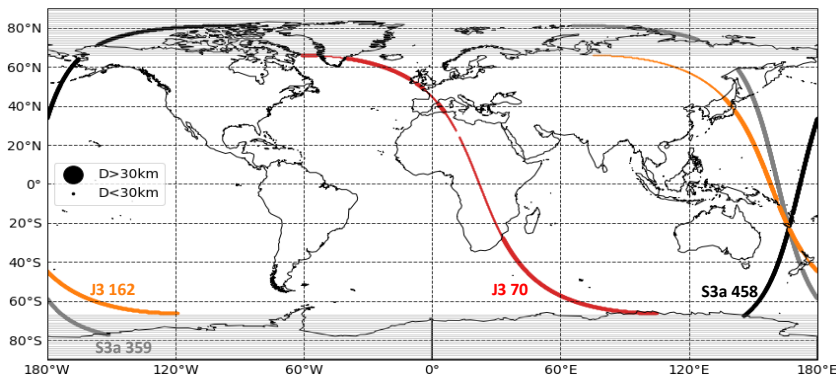
**Figure F1.** Comparison of global gravity field models with CalNaGeo measurements. / (a) Mean sea surface anomalies from CalNaGeo measurements during the GEOCEAN-NC cruise, expressed with respect to the altimeter comparison point (red dot on the map) / (b) Difference between CalNaGeo and the XGM2019e model with respect to the comparison point. / (c) Difference between CalNaGeo and the EGM08 model with respect to the comparison point. / (d) Difference between CalNaGeo and the EIGEN model with respect to the comparison point.

285 **Appendix G – Assessment of altimetry data quality in the lagoon**

The retracking provides the range by fitting a theoretical model on the radar echo recorded by the altimeter. The Mean Quadratic Error (MQE) parameter give an idea of the retracking process: the closer the MQE is to zero, the better the chosen model reproduce the measured waveform. So far, altimetry products do not give any indication of a valid or invalid MQE value. To get an idea of the "threshold" value of the MQE parameter that could discriminate valid or invalid ocean waveforms, we conducted an analysis on two Jason 3 and two Sentinel-3a tracks. For all cycles between 2016 and 2019, we extract along track 20Hz MQE parameter and compare them to the coastline distance.

295

300



305 **Figure G1.** Distance to nearest coastline from the along-track point of the 2 Jason and 2 Sentinel tracks used to analyse the MQE parameter. The big dots represent along-track points distant from more than 30km to the nearest coastline, and the small dots are point located on lands or less than 30km to the coastline. Note that to have a consistent comparison between both missions, Sentinel points located in polar areas (between -90°/-66° and 90°/66°) are not considered in the computation.

Commenté [CC15]: what is the dashed line?

Commenté [CC16R15]: It represents the mean value.

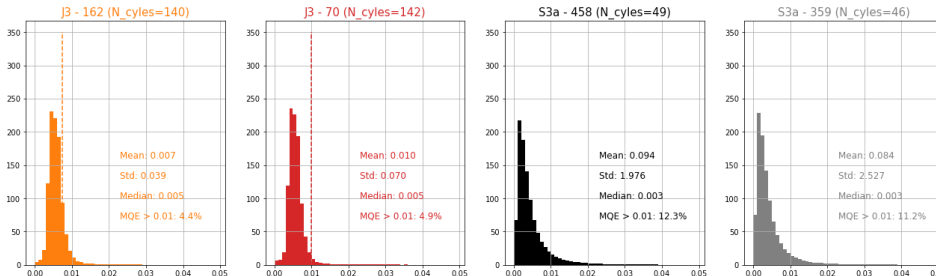


**Figure G2.** Statistics on the MQE values of points located more than 30km from the coast (considered as oceanic points). The dashed line represents the mean value.

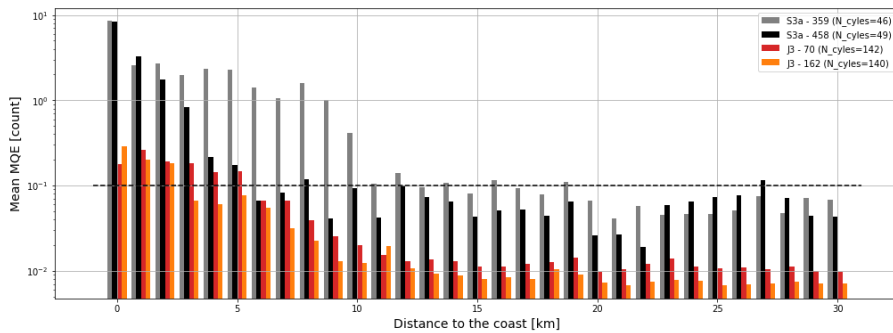


**Figure G3.** Mean values of MQE parameter function of the distance to the coast.

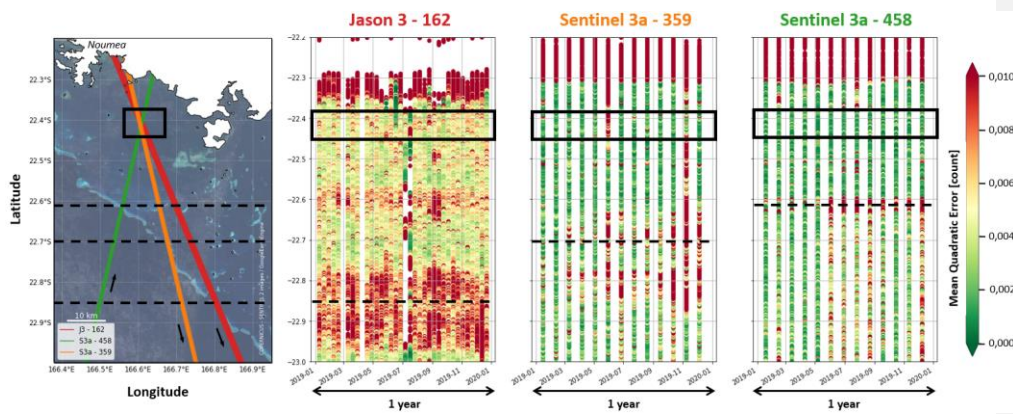
310 For Jason 3, our analysis shows that in the open ocean (*i.e.* distance to the coast > 30 km), the mean MQE parameter is less than or equal to 0.01 (Figure G2, red and orange). Along the Sentinel-3a tracks, this mean MQE value is more variable with a standard deviation of 2/2.5 (compared to 0.04/0.07 for Jason). However, the median is well below 0.01, suggesting that extreme values influence the estimate of the mean (Figure G2, grey and black). Approaching the coast, the MQE parameter increases significantly (Figure G3). In the 10/15 km range, the mean MQE tends towards 0.01 for Jason, but tends 0.1 for

315 Sentinel (Figure G3). We could therefore consider that MQE values greater than 0.01 could indicate an improper retracking and therefore potentially erroneous water depths. These preliminary results are strongly influenced by the tracks geometry, and a global analysis of all satellite passes would help to determine a more realistic threshold value for each mission.

However, to analyse our dataset, we considered that a MQE value above 0,01 may indicate a non-oceanic radar signal for

320 both Jason and Sentinel missions. Figure G4 shows the 20Hz along-track MQE parameter for the three tracks over the year 2019. There is about 3 times more Jason than Sentinel data, because of the difference in revisit period (respectively 9.9 and 27 days for Jason 3 and Sentinel satellites). We can note that for each track, the MQE parameter is higher and more variable at the coral reef overfly (black dotted line). Closer to the coast, the MQE parameter in the crossover area (black box) is mostly below 0.01, indicating that the waveforms retracking using the open ocean model is suitable for most passes. As the retracking

325 allows to determine the altimeter range, and thus to compute the altimeter Sea Surface Height, this result supports the idea that SSH altimetry data in our comparison area are reliable.



330 **Figure G4.** Along track Mean Quadratic Error (MQE) parameter for the 3 satellites passes that crosses in the lagoon during year 2019. The grey area represents the crossing area, and the black dotted lines the open-ocean/lagoon interface for each track.

## References

- 335 Aucan, J., Merrifield, M. A., and Pouvreau, N.: Historical Sea Level in the South Pacific from Rescued Archives, *Geodetic Measurements, and Satellite Altimetry*, *Pure Appl. Geophys.*, 174, 3813–3823, <https://doi.org/10.1007/s00024-017-1648-1>, 2017a.
- Aucan, J., Vendé-Leclerc, M., Dumas, P., and Bricquie, M.: Wave forcing and morphological changes of New Caledonia lagoon islets: Insights on their possible relations, *Comptes Rendus Geosci.*, 349, 248–259, <https://doi.org/10.1016/j.crte.2017.09.003>, 2017b.
- 340 Ballu, V., Gravelle, M., Wöppelmann, G., de Viron, O., Reibischung, P., Becker, M., and Sakic, P.: Vertical land motion in the Southwest and Central Pacific from available GNSS solutions and implications for relative sea levels, *Geophys. J. Int.*, 218, 1537–1551, <https://doi.org/10.1093/gji/ggz247>, 2019.
- Barbu, A. L., Laurent-Varin, J., Perosanz, F., Mercier, F., and Marty, J.-C.: Efficient QR sequential least square algorithm for high frequency GNSS precise point positioning seismic application, *Adv. Space Res.*, 61, 448–456, <https://doi.org/10.1016/j.asr.2017.10.032>, 2018.
- 355 Becker, M., Meyssignac, B., Letetrel, C., Llovel, W., Cazenave, A., and Delcroix, T.: Sea level variations at tropical Pacific islands since 1950, *Glob. Planet. Change*, 80–81, 85–98, <https://doi.org/10.1016/j.gloplacha.2011.09.004>, 2012.
- Blewitt, G., Kreemer, C., Hammond, W. C., and Gazeaux, J.: MIDAS robust trend estimator for accurate GPS station velocities without step detection, *J. Geophys. Res. Solid Earth*, 121, 2054–2068, <https://doi.org/10.1002/2015JB012552>, 2016.
- 350 Bonnefond, P., Exertier, P., Laurain, O., Ménard, Y., Orsoni, A., Jeansou, E., Haines, B. J., Kubitschek, D. G., and Born, G.: Leveling the Sea Surface Using a GPS-Catamaran, *Mar. Geod.*, 26, 319–334, <https://doi.org/10.1080/714044524>, 2003.
- Bonneton, P., Lefebvre, J.-P., Bretel, P., Ouillon, S., and Douillet, P.: Tidal modulation of wave-setup and wave-induced currents on the Aboré coral reef, New Caledonia, *J. Coast. Res.*, 762–766, 2007.
- 355 Chupin, C., Ballu, V., Testut, L., Tranchant, Y.-T., Calzas, M., Poirier, E., Coulombier, T., Laurain, O., Bonnefond, P., and Team FOAM Project: Mapping Sea Surface Height Using New Concepts of Kinematic GNSS Instruments, *Remote Sens.*, 12, 2656, <https://doi.org/10.3390/rs12162656>, 2020.
- DeMets, C., Gordon, R. G., and Argus, D. F.: Geologically current plate motions, *Geophys. J. Int.*, 181, 1–80, <https://doi.org/10.1111/j.1365-246X.2009.04491.x>, 2010.
- 360 Douillet, P.: Tidal dynamics of the south-west lagoon of New Caledonia: observations and 2D numerical modelling, *Oceanol. Acta*, 21, 69–79, [https://doi.org/10.1016/S0399-1784\(98\)80050-9](https://doi.org/10.1016/S0399-1784(98)80050-9), 1998.
- Garcin, M., Vendé-Leclerc, M., Maurizot, P., Le Cozannet, G., Robineau, B., and Nicolae-Lerma, A.: Lagoon islets as indicators of recent environmental changes in the South Pacific – The New Caledonian example, *Cont. Shelf Res.*, 122, 120–140, <https://doi.org/10.1016/j.csr.2016.03.025>, 2016.
- 365 Gravelle, M., Wöppelmann, G., Gobron, K., Altamimi, Z., Guichard, M., Herring, T., and Reibischung, P.: The ULR-repro3 GPS data reanalysis and its estimates of vertical land motion at tide gauges for sea level science, *Earth Syst. Sci. Data Discuss.*, 2022, 1–22, <https://doi.org/10.5194/essd-2022-235>, 2022.
- GRGS: Algorithmic documentation of the GINS software, 2018.

- 370 Hammond, W. C., Blewitt, G., Kreemer, C., and Nerem, R. S.: GPS Imaging of Global Vertical Land Motion for Studies of Sea Level Rise, *J. Geophys. Res. Solid Earth*, 126, <https://doi.org/10.1029/2021JB022355>, 2021.
- Heflin, M., Donnellan, A., Parker, J., Lyzenga, G., Moore, A., Ludwig, L. G., Rundle, J., Wang, J., and Pierce, M.: Automated Estimation and Tools to Extract Positions, Velocities, Breaks, and Seasonal Terms From Daily GNSS Measurements: Illuminating Nonlinear Salton Trough Deformation, *Earth Space Sci.*, 7, e2019EA000644, <https://doi.org/10.1029/2019EA000644>, 2020.
- 375 Hernández-Pajares, M., Juan, J. M., Sanz, J., and Orús, R.: Second-order ionospheric term in GPS: Implementation and impact on geodetic estimates, *J. Geophys. Res. Solid Earth*, 112, <https://doi.org/10.1029/2006JB004707>, 2007.
- Hersbach, H., Bell, B., Berrisford, P., Biavati, G., Horányi, A., Muñoz Sabater, J., Nicolas, J., Peubey, C., Radu, R., Rozum, I., Schepers, D., Simmons, A., Soci, C., Dee, D., and Thépaut, J.-N.: ERA5 hourly data on pressure levels from 1979 to present, Copernicus Climate Change Service (C3S) Climate Data Store (CDS), 2018.
- 380 Jouon, A., Lefebvre, J. P., Douillet, P., Ouillon, S., and Schmied, L.: Wind wave measurements and modelling in a fetch-limited semi-enclosed lagoon, *Coast. Eng.*, 56, 599–608, <https://doi.org/10.1016/j.coastaleng.2008.12.005>, 2009.
- Jullien, S., Aucan, J., Lefèvre, J., Peltier, A., and Menkes, C. E.: Tropical Cyclone Induced Wave Setup around New Caledonia during Cyclone COOK (2017), *J. Coast. Res.*, 95, 1454, <https://doi.org/10.2112/SI95-281.1>, 2020.
- 385 Kouba, J.: Implementation and testing of the gridded Vienna Mapping Function 1 (VMF1), *J. Geod.*, 82, 193–205, <https://doi.org/10.1007/s00190-007-0170-0>, 2008.
- Lemoine, J.-M., Biancale, R., Reinquin, F., Bourgeois, S., and Gégout, P.: CNES/GRGS RL04 Earth gravity field models, from GRACE and SLR data, 2019.
- Männel, B., Schöne, T., Bradke, M., and Schuh, H.: Vertical Land Motion at Tide Gauges Observed by GNSS: A New GFZ-TIGA Solution, Springer Berlin Heidelberg, Berlin, Heidelberg, 1–9, [https://doi.org/10.1007/1345\\_2022\\_150](https://doi.org/10.1007/1345_2022_150), 2022.
- 390 Martínez-Asensio, A., Wöppelmann, G., Ballu, V., Becker, M., Testut, L., Magnan, A. K., and Duvat, V. K. E.: Relative sea-level rise and the influence of vertical land motion at Tropical Pacific Islands, *Glob. Planet. Change*, 176, 132–143, <https://doi.org/10.1016/j.gloplacha.2019.03.008>, 2019.
- 395 Marty, J. C., Loyer, S., Perosanz, F., Mercier, F., Bracher, G., Legresy, B., Portier, L., Capdeville, H., Fund, F., Lemoine, J. M., and Biancale, R.: GINS: The CNES/GRGS GNSS scientific software, in: ESA Proceedings WPP326, 3 rd International Colloquium Scientific and Fundamental Aspects of the Galileo Programme, Copenhagen, Denmark, 2011.
- Nerem, R. S. and Mitchum, G. T.: Estimates of vertical crustal motion derived from differences of TOPEX/POSEIDON and tide gauge sea level measurements, *Geophys. Res. Lett.*, 29, 40-1-40–4, <https://doi.org/10.1029/2002GL015037>, 2002.
- Okada, Y.: Surface deformation due to shear and tensile faults in a half-space, *Bull. Seismol. Soc. Am.*, 75, 1135–1154, <https://doi.org/10.1785/BSSA0750041135>, 1985.
- 400 Pavlis, N. K., Holmes, S. A., Kenyon, S. C., and Factor, J. K.: The development and evaluation of the Earth Gravitational Model 2008 (EGM2008), *J. Geophys. Res. Solid Earth*, 117, <https://doi.org/10.1029/2011JB008916>, 2012.
- Peltier, W. R., Argus, D. F., and Drummond, R.: Space geodesy constrains ice age terminal deglaciation: The global ICE-6G\_C (VM5a) model, *J. Geophys. Res. Solid Earth*, 120, 450–487, <https://doi.org/10.1002/2014JB011176>, 2015.

405 Saastamoinen, J.: Atmospheric Correction for the Troposphere and Stratosphere in Radio Ranging Satellites, in: Geophysical Monograph Series, edited by: Henriksen, S. W., Mancini, A., and Chovitz, B. H., American Geophysical Union, Washington, D. C., 247–251, <https://doi.org/10.1029/GM015p0247>, 1972.

Vondrak, J.: Problem of Smoothing Observational Data II, *Astron. Institue Czechoslov. Acad. Sci. Praha*, 28, 84–89, 1977.

410 Weatherall, P., Marks, K. M., Jakobsson, M., Schmitt, T., Tani, S., Arndt, J. E., Rovere, M., Chayes, D., Ferrini, V., and Wigley, R.: A new digital bathymetric model of the world's oceans, *Earth Space Sci.*, 2, 331–345, <https://doi.org/10.1002/2015EA000107>, 2015.

Zingerle, P., Pail, R., Gruber, T., and Oikonomidou, X.: The combined global gravity field model XGM2019e, *J. Geod.*, 94, 66, <https://doi.org/10.1007/s00190-020-01398-0>, 2020.